PHYSICAL REVIEW B **96**, 054110 (2017)

Computer simulation of thermal conductivity in vulcanized polyisoprene at variable strain and temperature

Sven Engelmann,[*] Jan Meyer, and Reinhard Hentschke
Physics Department, University of Wuppertal, D-42097 Wuppertal, Germany

(Received 6 April 2017; revised manuscript received 11 July 2017; published 14 August 2017)

We study the thermal conductivity tensor in an atomistic model of vulcanized cis-1,4-polyisoprene (PI) rubber via molecular dynamics simulations. Our polymer force field is based on V. A. Harmandaris *et al.* [J. Chem. Phys. **116**, 436 (2002)], whereas the polymerization algorithm follows the description in J. Hager *et al.* [Macromolecules **48**, 9039 (2015)]. The polymer chains are chemically cross linked via sulfur bridges of adjustable cross-link density. A volume-conserving uniaxial strain of up to 200% is applied to the systems. The widely used GROMACS simulation package is adapted to allow using the Green-Kubo approach to calculate the thermal conductivity tensor components. Our analysis of the heat flux autocorrelation functions leads to the conclusion that the thermal conductivity in PI is governed by short-lived phonon modes at low wave numbers due to deformation of the monomers along the polymer backbone. Applying uniaxial strain causes increased orientation of monomers along the strain direction, which enhances the attendant thermal conductivity component. We find an exponential increase of the conductivity in stretch direction in terms of an attendant orientation order parameter. This is accompanied by a simultaneous decline of thermal conductivity in the orthogonal directions. Increase of the cross-link density only has a weak effect on thermal conductivity in the unstrained system, even at high cross-link density. In the strained system we do observed a rising thermal conductivity in the limit of high stress. This increase is attributed to enhanced coupling between chains rather than to their orientation.

DOI: 10.1103/PhysRevB.96.054110

I. INTRODUCTION

Amorphous polymer materials possess rather small thermal conductivities of around 0.1 W/mK. In the case of elastomers this material parameter is of particular interest, because of the intricate coupling between operating conditions and heat buildup. For instance, the operating temperature of automobile tires strongly affects their performance, e.g., grip or rolling resistance. When a tire, which is a complex multimaterial product, is designed using finite-element solvers for the macroscopic material equations, parameters such as the thermal conductivity (coefficients) are inserted from some standard source. This is not always the preferred method, because a material parameter is not a constant. During the past decade it has become possible to obtain material parameters via atomistic computer simulation. This approach provides a direct link between the parameter of interest, a material's chemical structure, and thermodynamic conditions. The method of choice for the calculation of transport properties is molecular dynamics, which means solving the atomic equations of motion.

A fair number of simulation studies in the past have focused on single polymer chains, in particular polyethylene models. This is because experimental studies have shown that strong uniaxial orientation of polymers can give rise to a pronounced increase of thermal conductivity in chain direction attributed to phonons along the backbone [1]. Using equilibrium and nonequilibrium molecular dynamics Wang and Li [2] study a one-dimensional particle chain, which they analyze using a simple mode-coupling theory. They find three types of thermal conduction: a logarithmic divergence with system sizes for large transverse coupling, a 1/3 power law at intermediate coupling, and a 2/5 power law at low temperatures and weak coupling. A similar single-chain study, based on polyethylene, is described by Henry and Chen [3], who study the increase of thermal conductivity with chain length. Two recent studies in the same category are reported by Hu *et al.* [4] and Lin *et al.* [5]. Hu *et al.* compute the thermal conductivity of a single polymer chain via the Green-Kubo approach as well as a nonequilibrium molecular dynamics simulation method. They too focus on the unexpectedly large thermal conductivity of isolated united-atom polyethylene chains. Lin *et al.* use nonequilibrium molecular dynamics to also study thermal conductivity along isolated polyethylene chains in terms of chain length and strain.

Thermal conductivity in bulk isotropic polymer samples, e.g., amorphous polyvinyl chloride, poly(methyl methacrylate), polystyrene, or polycarbonate, is much less pronounced—albeit technically more important. A number of molecular dynamics simulation studies do exist, which focus on such systems. Lussetti *et al.* [6] present a nonequilibrium molecular dynamics simulation study on the thermal conductivity in bulk polymer samples of amorphous polyamide-6,6. Four separate models, differing in their number of high-frequency degrees of freedom, are compared. The authors find that the thermal conductivity systematically depends on the number of degrees of freedom. The authors also show that the thermal conduction is faster parallel to the drawing direction than perpendicular to it. Algaer *et al.* [7] investigate the thermal conductivity of stretched amorphous atactic polystyrene swollen in supercritical carbon dioxide over a wide temperature, pressure, and concentration range. Liu and Yang [8] use an all-atom molecular dynamics simulation of polyethylene to study the tuning of polymer thermal conductivity via mechanical strain. These authors do show that the thermal conductivity increases with increasing strain and the enhancement is larger (about 20%) when the polymer is stretched more slowly. The two strain rates in this

---

[*] Corresponding author: s.engelmann@uni-wuppertal.de

study differ by a factor of ten. Decreasing the strain rate also increases the orientation order, which, as we also find in this work, correlates with the thermal conductivity. In addition, it is observed that the thermal conductivity is affected by molecular weight. Increasing the chain length from 200 to 400 results in a 20% increase of thermal conductivity. Zhao *et al.* [9] apply united-atom nonequilibrium molecular dynamics simulations to predict the thermal conductivity for amorphous polyethylene at room temperature and chain lengths ranging from 4 to 1260. The attendant system densities vary strongly. Whereas the short molecules form a gas, the long chains do form a condensed amorphous phase. Accordingly the authors observe collision-dominated thermal conductivity at low densities and phonon-dominated thermal conductivity in the condensed phase. The effect of a confining geometry on the thermal conductivity of polyamide-6,6 oligomers between graphene sheets, using reverse nonequilibrium molecular dynamics, is discussed by Alaghemandi *et al.* [10]. Their results show that the coefficient of thermal conductivity parallel to the confining surfaces depends on the intersurface distance and is much higher than that of the bulk polymer [11]. Rossinsky and Müller-Plathe [12] employ a nonequilibrium simulation study of the heat conductivity in crystalline polystyrene focusing on anisotropy. Ni *et al.* [13] study the thermal conductance across different interfaces consisting of oriented single-crystal diamond surfaces and covalently bonded as well as completely aligned polyethylene chains by molecular dynamics simulation. In addition, effects of defects and cross linking are analyzed. Varshney *et al.* [14] present a study of a cross-linked polymer system, an epoxy-based thermoset polymer. The thermal conductivity is calculated using both nonequilibrium as well as equilibrium molecular dynamics techniques. A recent simulation study on polyisoprene rubber, the system we focus on in this work, is that of He *et al.* [15]. The authors study two structurally different systems, i.e., isoprene oligomer samples consisting of short disordered chains, containing 10 monomer units each, without chemical cross links and a quasicrystalline sample of straight chains, in order to estimate the anisotropy of the thermal conductivity. In contrast to the present study the authors do not use a united-atom model but include the hydrogen atoms explicitly. We comment on this technical point later in this text. The authors observe, as we do also, that the thermal conductivity is enhanced along the direction of the chains in the highly ordered system. Finally we mention a recent review by Algaer and Müller-Plathe [16] on molecular dynamics calculations of the thermal conductivity in molecular liquids, polymers, and carbon nanotubes.

Experimental measurements of thermal conductivity in elastomers started to appear in the 1920s and 1930s, motivated by the increased use of these materials in technical applications involving high-frequency deformations with attendant heat generation. One example is the work of Barnett [17], who already studied the effect of fillers on thermal conductivity. Another subsequent paper by Dauphinee *et al.* [18] discusses the thermal conductivity of elastomers as a function of strain and temperature. Two early reviews on the experimental data available on the thermal conductivity of polymers up until 1966 are the papers by Anderson [19] and, focusing on rubber, Carwile and Hoge [20]. One of the references included in this second review is by Tautz [21], which explicitly addresses the dependence of the thermal conductivity of a number of rubbers on strain. Subsequent work by Hands and Horsfall [22] describes measurement techniques and measurements of the thermal conductivity of rubber specimens containing carbon black filler. In addition, Hands [23] investigates the effect of equibiaxial orientation on the thermal conductivity of a series of natural rubber compounds. Finally, the paper by Bhowmick and Pattanayak [24] is a more recent study of the thermal conductivity, heat capacity, and diffusivity in various rubbers, i.e., poly(butadiene-co-styrene), polychloroprene, and cis-1,4-polyisoprene, from 60 to 300 K, i.e., through the respective glass transitions.

In this work we study the thermal conductivity tensor in a united-atom model of cis-1,4-polyisoprene (PI) rubber via molecular dynamics simulations. Our polymer force field is based on Harmandaris *et al.* [25], whereas the polymerization algorithm follows the description in Hager *et al.* [26]. On this basis we study a number of different systems distinguished by their polymer molecular weight, different chemical cross link, i.e., sulfur bridge, densities, and temperature. The systems are subjected to volume-conserving uniaxial strain of up to 200%. For this purpose the widely used GROMACS simulation package [27] is adapted allowing us to employ the Green-Kubo approach to the calculation of the thermal conductivity tensor components $\Lambda_{\alpha\beta}$. We analyze the the heat flux autocorrelation functions and come to the conclusion that the thermal conductivity in PI is governed by short-lived phonon modes at low wave numbers. Comparison with experimental results from vibration spectroscopy suggests that physically these modes correspond to deformations of the monomers along the polymer backbone. Application of uniaxial strain causes increased orientation of the monomers in strain direction, which enhances conductivity along this direction. We find an exponential dependence of this thermal conductivity component on a suitably defined order parameter. This is accompanied by a simultaneous decline of thermal conductivity in the orthogonal directions. If the cross-link density is increased in the unstrained system, we do observe (on average) a small rise of the thermal conductivity, which qualitatively is in accord with experimental data. A more noticeable increase in response to higher cross-link density is observed when strain is applied, but only at the highest stresses. This increase cannot be attributed to orientation but appears to be due to enhanced coupling between chains.

II. SIMULATION DETAILS

The bulk polymer system is polymerized from a liquid of monomers using the approach presented in detail by Hager *et al.* [26], which allows for variable chain length and number of chains. The polymer force field parameters are those of Harmandaris *et al.* [25]. However, we do not include long-range dispersion corrections. In addition we also do not use constraints for the internal bonds since this leads to problems during deformation of the system. These adjustments give rise to density deviations which we reduce by decreasing all σ parameters by 2% (relative to the values in the aforementioned reference).

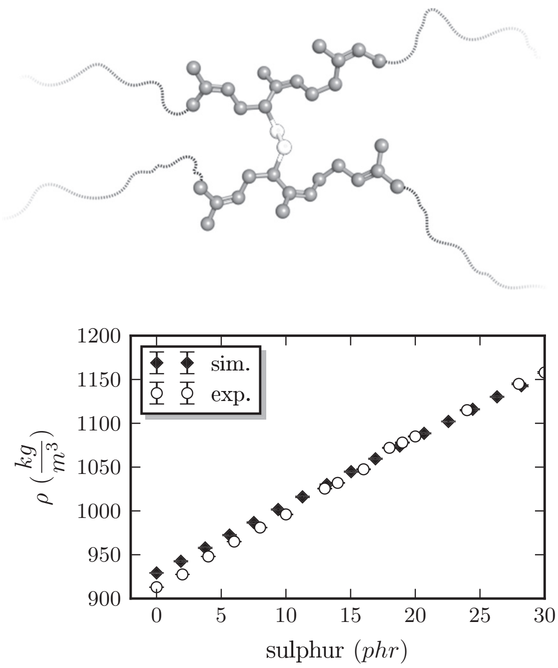

FIG. 1. Top: Type and position of the sulfur bridges in this work. Bottom: Bulk-polymer density vs concentration of sulfur in phr [parts (by weight) per hundred rubber] at $T = 300$ K and $P = 1$ bar. This systems consists of 40 polymer chains containing 200 monomers each. The experimental densities are taken from McPherson [28].

The polymers are cross linked by sulfur bridges consisting of two sulfur atoms each. The cross links are uniformly distributed in the system subject to the constraint that all polymer ends are joined to a neighboring chain via a sulfur bridge. The latter avoids dangling polymer ends. An additional restriction is that a chain cannot be cross linked to itself. The sulfur bridges are described by the Amber94 force field [29]. This part of our parametrization is validated by comparing the classical approach used here to Carr-Parinello molecular dynamics calculations on selected small compounds [30]. Quantities used for comparison include bond lengths, valence angles, and torsion angles. Deviations for the former two are less than 10% whereas the torsion angles deviate, not unexpectedly, by about 20% mostly due to small compound size. Figure 1 shows the dependence of the system‘s density on cross-link concentration in comparison to experimental data. This system consists of 40 polymer chains containing 200 monomers each. The overall agreement is quite good. In order to obtain the strain dependence of the components of the thermal conductivity tensor, $\Lambda_{\alpha\beta}$, we use Eq. (A21) discussed in Appendix A. Additional computational details are compiled in this appendix as well as in Appendix B.

Prior to the actual measurement of the thermal conductivity the system is preconditioned during two initial volume-conserving strain cycles, using a constant strain rate. The strain amplitude is 200% (unless stated otherwise) and the attendant strain cycle frequency is $1/12.5\,\mathrm{ns}^{-1}$. Subsequently the actual data are taken during a final stretching of the system. Unless stated otherwise the temperature is 300 K and the pressure, in the case of *NPT* simulations (particle number, pressure, and temperature are kept constant), is 1 bar. Each data point encompasses two steps: (i) an equilibration time of about 500 ps at *NPT* conditions keeping the strain, u, constant; (ii) a subsequent NVT simulation (particle number, volume, and temperature are kept constant), using a time step of 2.5 fs, during which the components of the heat current according to Eq. (A10) are determined.

III. RESULTS

Figure 2 is an example showing a particular system in the undeformed state as well as at 150% strain. The system consists of 20 polyisoprene (PI) chains containing 250 monomers each cross linked via 500 disulfide bonds. The edge length of the undeformed simulation cell is $L_x = L_y = L_z \approx 8.53$ nm. A number of chains are shown in color to make the effect of strain on the chain conformations visible.

The dependence of chain orientation on strain is depicted in Fig. 3, showing the orientation distribution function, $f(\theta)$, for different strain values, u. The angle θ is the angle between a C-C double bond and the z or stretch direction. We return to this figure below.

The upper panel of the next figure, Fig. 4, shows the mean square polymer segment end-to-end distance along a particular direction α, $\langle R_\alpha^2 \rangle$, divided by the attendant length of the simulation box, L_α, vs strain, u. In the case of an affine deformation this ratio is constant. The bottom panel of this figure shows c_α defined via $\langle R_\alpha^2 \rangle = c_\alpha b^2 (4n)$, where b^2 is the mean square bond length in a monomer, and $4n$ is the total number of bonds. Here $b \approx 0.15$ nm, and $n = 250$. Notice that

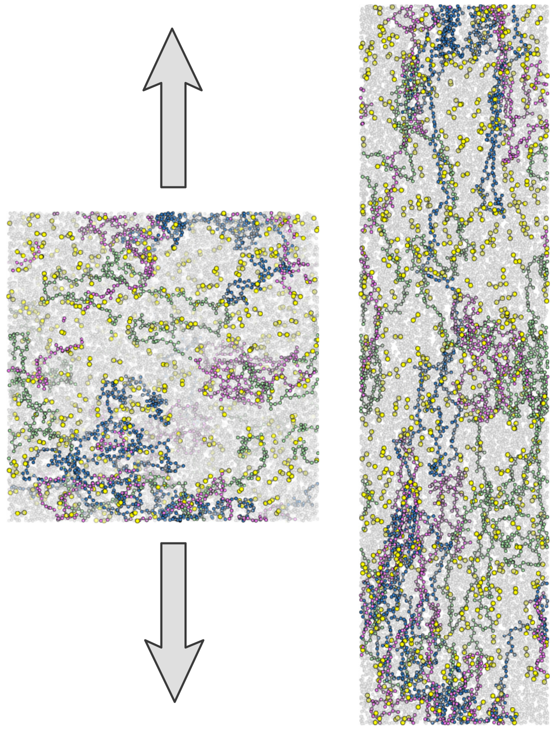

FIG. 2. Example showing one particular system in the undeformed state (left) and at 150% strain (right). Selected polymer chains are highlighted in different colors. Yellow dumbbells indicate sulfur cross links. The system consists of 20 PI chains containing 250 monomers each and 500 sulfur cross links.

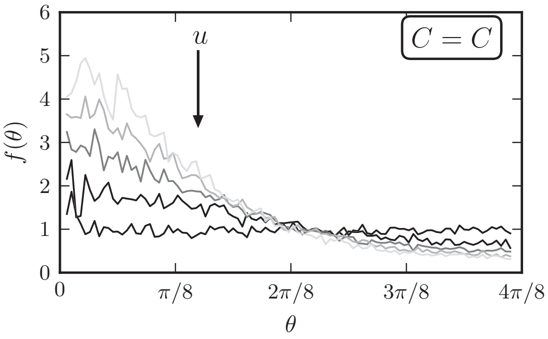

FIG. 3. (Double) bond orientation distribution functions at different strain values, $u = [0.0, 0.5, 1.0, 1.5, 2.0]$. Notice that θ refers to the angle between the double bond and the direction of stretch.

at zero strain, i.e., $u = 0$, $c_\alpha \approx 2$, and thus the characteristic ratio we obtain is close to 6. This value is somewhat higher than values reported in Ref. [31] (between 4 and 5), albeit at a higher temperature, i.e., at 413 K instead of the 300 K in the present study. The two cases, i.e., no cross links and phr = 9.41 [where phr is parts (by weight) per hundred rubber], refer to the cases when the aforementioned polymer segment encompasses the entire polymer and the segment length between sulfur cross links, respectively. The two lengths are very different, which here however does not have a clearly discernible effect on c_α at $u = 0$. For $u > 0$ we notice first that $\sqrt{\langle R_\alpha^2\rangle}/L_\alpha$ shows a slight increase in the system with no cross links (notice that the frequency of deformation is rather high—a point to which we return below). However, the error bars are quite large due to the limited number of polymer chains entering into the average. The cross-linked systems are very different in this respect, which yields smoother data as well as a reduced maximum strain. In the direction of stretch c_z increases more strongly when there are no cross links. The corresponding quantities in the orthogonal directions, on the other hand, differ only slightly.

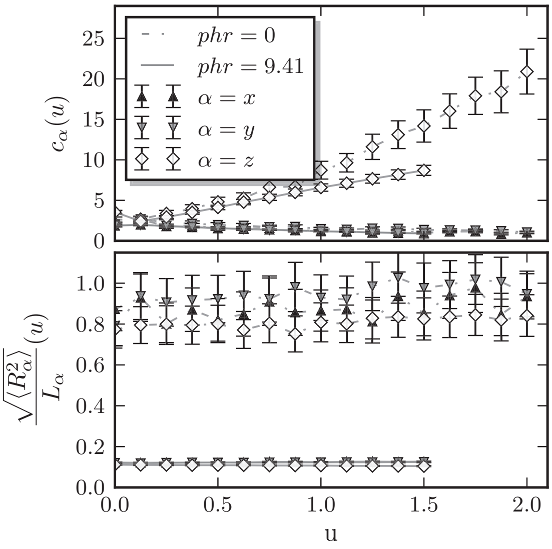

FIG. 4. Top: Root mean square of R_α, divided by the attendant box dimension, L_α, vs strain, u. Bottom: c_α vs u corresponding to the panel above.

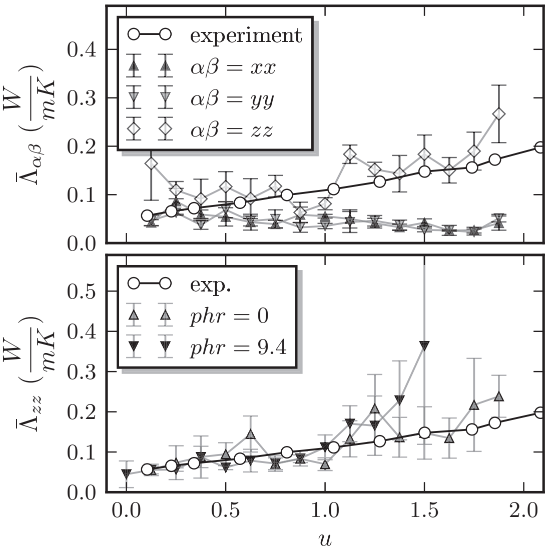

FIG. 5. Top: Diagonal components of the thermal conductivity tensor at $T = 300$ K vs strain, u. The experimental data measured along the long direction are taken from Tautz [21]. The number of cross links is about 100 or about 1.9 phr. Bottom: Thermal conductivity along the stretch direction for systems with very different cross-link concentrations. Notice that the over bars indicate averages over four independent measurements.

Figure 5 shows the diagonal components of the thermal conductivity tensor at $T = 300$ K vs strain, u. The strain is applied along the z direction. The experimental data measured along this direction are taken from Tautz [21]. Notice the clearly discernible increase of the thermal conductivity in the long direction in good accord with the experimental data. The bottom panel illustrates that the increase of Λ_{zz} above $u = 1$ is more pronounced when the cross-link density is increased. In contrast, the thermal conductivity in the orthogonal direction exhibits an apparent decline over the entire strain range. The same is observed by Liu and Yang [8] in their study on polyethylene. Corresponding to the top panel in this figure, Fig. 6 shows autocorrelation functions of the heat current components $J_\alpha(t)$ for different strain values. The autocorrelation function in the bottom panel is for $\alpha = z$, where z is the direction of stretch. The upper curve is for a large strain, i.e. $u \approx 1.6$, whereas the lower curve is for a small strain, i.e., $u \approx 0.4$. All discernible features of the curves in the two cases are quite similar. The curves differ by magnitude rather than shape. The same is true for the corresponding autocorrelation functions in the top panel, which are for $\alpha = x$. Corresponding to the autocorrelation functions in Fig. 6, Fig. 7 shows $\Lambda_{xx}(t')$ and $\Lambda_{zz}(t')$. Here t' is the upper limit of the integral in Eq. (A21) (replacing ∞). The figure provides a connection between the integration range and the attendant contribution from that range to the thermal conductivity. Notice that the thermal conductivity components require integration of the autocorrelation function out to several 10^{-1} ps to approach their asymptotic values.

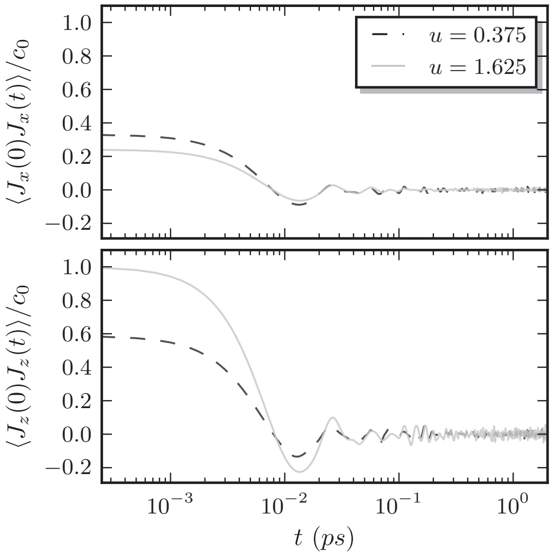

FIG. 6. Time autocorrelation functions of the heat current components $J_\alpha(t)$ for different strain values. Top: $\alpha = x$. Bottom: $\alpha = z$, where z is the direction of stretch. The temperature is 300 K in all cases. Notice that the curves are all normalized to $c_0 = \langle J_z(0)J_z(0)\rangle$ at $u = 1.625$.

In the following we want to elucidate the molecular mechanisms underlying the results shown in Figs. 5 through 7. The current components $J_\alpha(t)$ in Eq. (A10) are the sum of two terms. For the moment we focus on the second, which turns out to be the dominant term in the present system. In order to understand the basic shape of the autocorrelation functions in Fig. 6, we construct a simple example. Let $x(t) = \sin(\omega t)$ be the displacement of a one-dimensional harmonic oscillator of unit mass at time t. The corresponding force is $f(t) = -\omega^2 x(t)$ and the velocity is $v(t) = \omega\cos(\omega t)$. The product, i.e., $J^{(2)}(t) = x(t)f(t)v(t)$, is an extremely simplified analog to the second term on the right-hand side of Eq. (A10). We may construct a likewise simple autocorrelation function defined via

$$\langle J^{(2)}(0)J^{(2)}(t)\rangle = \frac{\omega}{2\pi}\int_0^{2\pi/\omega} dt'\, J^{(2)}(t')J^{(2)}(t'+t)e^{-t/\tau}, \quad (1)$$

describing a collection of oscillators with different phases over which we average. The exponential function is a simple means to model the decay of the oscillator excitations. Figure 8 shows the normalized function $\langle J^{(2)}(0)J^{(2)}(t)\rangle$ according to this equation for $\omega = 1$ and $\tau = 1$. In general the first minimum (or "negative correlation") will appear at $t \approx 1/\omega$. Notice that the overall shape of this function roughly mimics the shape of the autocorrelation functions in Fig. 6.

We test this concept using examples of increasing complexity. The first example is the Lennard-Jones (LJ) system; i.e., the interparticle potential is $u(r) = 4\epsilon[(\sigma/r)^{12} - (\sigma/r)^6]$. Figure 9 shows heat flux autocorrelation functions obtained

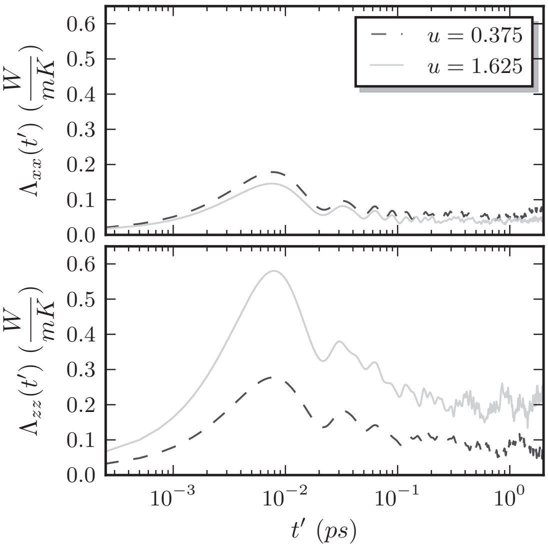

FIG. 7. $\Lambda_{xx}(t')$ (top) and $\Lambda_{zz}(t')$ (bottom) vs t', corresponding to the autocorrelation functions of the previous figure. The quantity t' is the upper limit of the integral in Eq. (A21) and the temperature is 300 K.

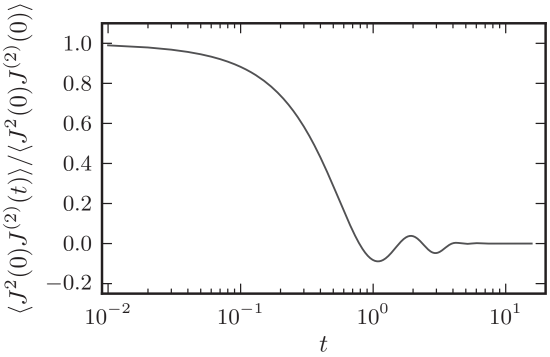

FIG. 8. The function of Eq. (1) for $\omega = 1$ and $\tau = 1$.

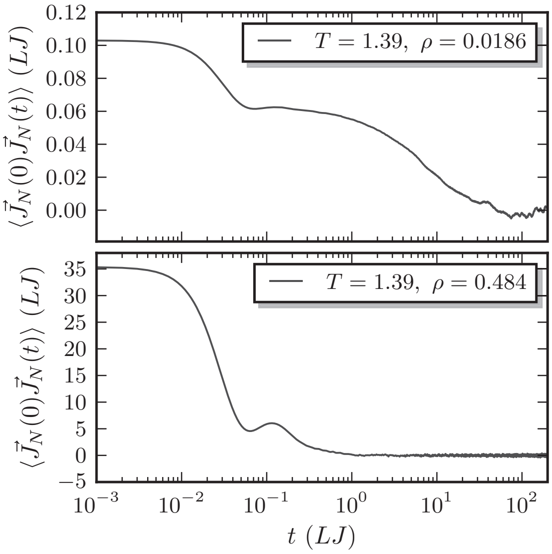

FIG. 9. Heat flux autocorrelation functions obtained in the LJ system at two different state points, i.e., $T = 1.39$, $\rho = 0.484$ and $T = 1.39$, $\rho = 0.0186$. The index N means that a factor $\sqrt{V/(3T^2)}$ is absorbed into each $\vec{J}$; i.e., the area under the curves is the respective isotropic thermal conductivity in LJ units.

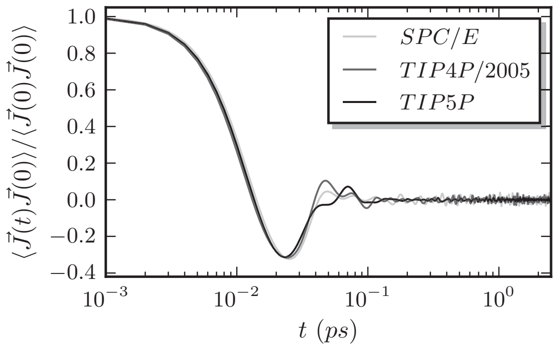

FIG. 10. Normalized heat flux autocorrelation functions obtained for the three indicated rigid water models at $T = 300$ K and ambient pressure using molecular dynamics simulations.

at two state points, i.e., $T = 1.39$, $\rho = 0.484$ and $T = 1.39$, $\rho = 0.0186$. Here ρ is the particle number density and we use LJ units throughout the remainder of this example (i.e., energy is in units of ϵ, length is in units of σ, time is in units of $\tau_{LJ} = \sqrt{m\sigma^2/\epsilon}$, where m is the particle mass, and temperature is in units of ϵ/k_B, where k_B is Boltzmann's constant). Notice that the critical temperature and density of the LJ system are about 1.32 and 0.31, respectively.

Neither of the two autocorrelation functions exhibits negative correlations. But both do show a local minimum at $t \approx 0.07$, which at the low density is very shallow. Can we interpret these minima in the above sense? Even the low-density gas, at any particular time, does contain a small fraction of dimers, i.e., momentarily bound particles (in the sense of the cluster expansion picture). If we expand the above LJ potential at its minimum to second order in the displacement, then we find that the frequency of the corresponding oscillator is $\omega = 6 \times 2^{1/3}$ and thus $1/\omega \approx 0.13$ (in LJ units). Even though this value overestimates the position of the above minimum by a factor of two, considering the crudeness of our estimate, we discern the traces of our above idea. Notice that our harmonic-oscillator assumption in the present case is quite rough and, especially at the higher density, most clusters do contain more than two particles. This means that a particle oscillating in a cage of nearest neighbors is possibly a more accurate description than dimer oscillations. In addition energy transfer is dominated by single-particle collisions at the low density, which lead to the long relaxation time exhibited by the autocorrelation function in the upper panel in Fig. 9 (cf. chapter 9 in Ref. [32]). We note that Zhao *et al.* [9] (cf. our introduction) simulate the thermal conductivity in systems of oligoethylene over a range of densities depending on the oligomer's lengths. They observe low thermal conductivity at low densities or small oligomers and larger thermal conductivity at high densities or long chains. This observation is attributed to collision dominance at the low densities vs phonon dominance at high densities. However, no further analysis is given in support of this conclusion.

Our second example is liquid water. Figure 10 shows normalized heat flux autocorrelation functions obtained for three frequently studied water models (simple point charge/extend [33], transferrable intermolecular potential 4 point/2005 [34], and transferrable intermolecular potential 5 point [35]) describing the water molecule with increasing detail. In this system we observe the pronounced negative correlations akin to those observed for PI (cf. Fig. 6). Here the first minimum is located at $t \approx 2.5 \times 10^{-14}$ s. Based on our above simple oscillator model we obtain $\omega \approx 1/2.5 \times 10^{-14}$ s and converting this ω into a wave number we find $\tilde{\nu} = (2\pi)^{-1}(\omega/c) \approx 210\text{cm}^{-1}$, where c is the speed of light. The infrared absorption spectrum of liquid water indeed shows a broad peak located at this wave number, which is attributed to a complicated "rocking motion" or libration of the water molecule [36].

It is worth noting in this context that the isochoric heat capacity of liquids usually is close to $3k_B$ (we note also that PI is no exception in this respect; cf. [37]). Heat capacity and thermal conductivity are intimately related (cf. for instance Sec. 9.2.c in Ref. [32]). For instance, Lussetti *et al.* [6] study the correlated increase of both quantities as a function of the degrees of freedom in their model. This is a subtle point when using classical force field simulations, because high-frequency modes involving single or only a few light atoms (such as C-H vibrations) are not classically excited at the temperatures of interest. On the other hand, the experimental isochoric heat capacity of for instance liquid water near the melting point is very close to $3k_B$ (per atom). This shows that the high frequency vibration modes of water in the gas phase are "softened" in the condensed state due to the coupling between the molecules giving rise to different vibrational modes. Therefore even classical force field models yield quite reasonable descriptions of its thermodynamic and transport properties. Probably it is fair to say that united-atom models, which must however include hydrogen atoms involved in hydrogen bonds explicitly, are very reasonable models in the present context.

We now apply our idea that the dominant cause of heat flux is due to low wave number oscillatory modes to PI. Here the first minimum is located at $t \approx 1.2 \times 10^{-14}$ s and thus $\omega \approx 1/1.2 \times 10^{-14}$ s. Converting this ω into a wave number we find $\tilde{\nu} = (2\pi)^{-1}(\omega/c) \approx 440\text{cm}^{-1}$. Nallasamy *et al.* [38] have studied PI using vibrational spectroscopy. They assign a large number of different modes to their respective wave numbers. Wave numbers at around $440\,\text{cm}^{-1}$ they identify with C-C-C deformation modes. We therefore conclude that in the case of PI the components of the heat capacity tensor are governed by short-lived phonon modes due to deformations of the monomers, i.e., deformations in chain direction.

We note that the quantity $(1/2)\hbar\omega/k_B$, where $(1/2)\hbar\omega$ is the zero-point energy of a one-dimensional quantum oscillator with the frequency ω, is about 300 K if ω is equal to the above value. This is consistent with the underlying assumption that a classical force field approach at the temperatures used in this study is reasonable, considering the quantum nature of the phenomenon.

Thus far we have focused on the second term on the right-hand side in the heat flux equation (A10). We can of course compare the two relative contributions of the two terms to the thermal conductivity. It turns out that the second term in the present case dominates by far; i.e., a plot of the heat flux autocorrelation function neglecting the first term is virtually identical to the full results in Fig. 6. Notice also that L/c_s, which is the time it takes a sound wave with the speed c_s to travel through a simulation box of linear size L, due to its periodicity, is much larger than the above value for $1/\omega$. And

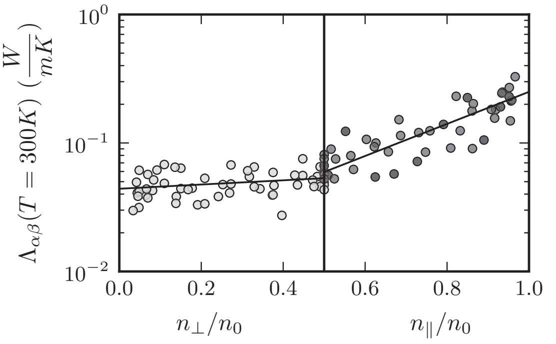

FIG. 11. $\Lambda_{zz}(u)$ vs $n_{\parallel}(u)/n_o$ (right side) and $[\Lambda_{xx}(u)+\Lambda_{yy}(u)]/2$ vs $n_{\perp}(u)/n_o$ (left side) based on the simulation results shown in Figs. 3 and 5 (upper panel). The lines through the data are explained in the text.

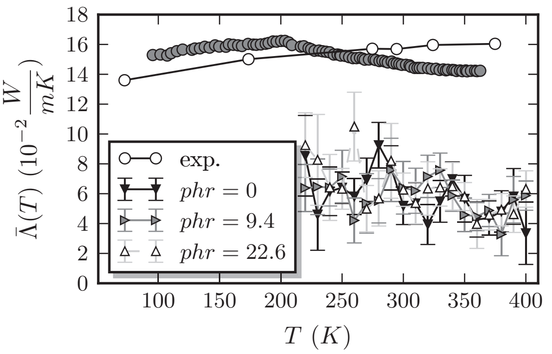

FIG. 12. Temperature dependence of the thermal conductivity for $u=0$. The three simulated systems are distinguished by the sulfur content. The experimental data [20] encompass hard and soft rubber, where hard rubber (open circles) corresponds to about 47 phr of sulfur and soft rubber (filled circles) means about 2.5 phr of sulfur, respectively.

even more importantly, this time depends on L, which does vary in our study without however causing a discernible effect on the aforementioned negative correlations.

Finally we discuss the effect of straining the polymer system on the thermal conductivity components as shown in Fig. 5. Stretching of the elastomer results in an increased alignment of polymer backbone segments along the direction of stretch. Based on our above interpretation we expect this to enhance the heat transport along the direction of stretch. Simultaneously the conductivity in the orthogonal directions should diminish. There are two orthogonal directions vs one parallel direction, so that the increase along the deformation direction is more pronounced.

We may employ the orientation distribution function, $f(\theta)$, introduced in the context of Fig. 3, to correlate the number of monomers oriented along a certain solid angle with the diagonal components of the thermal conductivity tensor obtained at the same values of u. The relative number of monomers possessing an angle θ, i.e., the angle of the double bond relative to the z axis, less than $\pi/3$ is given by

$$n_{\parallel}(u)/n_o = \int_0^{\pi/3} d\theta \sin\theta f(\theta;u), \tag{2}$$

where n_o is the total number of monomers in the system. The quantity $n_{\perp}(u)=n_o-n_{\parallel}(u)$ is the corresponding number of monomers outside this solid angle, i.e., in the range $\pi/3<\theta\leqslant\pi/2$. Notice that if $f(\theta;u)=1$, i.e., the distribution is uniform, this yields $n_{\parallel}(u)/n_o=n_{\perp}(u)/n_o=1/2$ (this is why above we choose $\pi/3$). Notice also that we use the normalization $\int_0^{\pi/2} d\theta \sin\theta f(\theta;u)=1$. It is useful to express $f(\theta;u)$ via the (normalized) fit function $f(\theta;u)=(a/\sinh[a])\cosh[-a\cos\theta]$, where $a=a(u)$ is an adjustable parameter for a fixed value of u. Notice that with this function $n_{\parallel}(u)/n_o=1-1/(2\cosh[a/2])$. Adjusting the fit function to the data shown in Fig. 3, including angular distributions obtained at additional u values not shown explicitly, we obtain a series of attendant values $a(u)$ and correspondingly values for $n_{\parallel}(u)$. Figure 11 is a plot of $\Lambda_{zz}(u)$ vs $n_{\parallel}(u)/n_o$ as well as $[\Lambda_{xx}(u)+\Lambda_{yy}(u)]/2$ vs $n_{\perp}(u)/n_o$. We notice first that $\Lambda_{zz}(u)$ increases with increasing $n_{\parallel}(u)/n_o$. The line through the data is a fit based on $\ln[\Lambda_{zz}(u)/\Lambda_{zz}(0)]=b[n_{\parallel}(u)/n_o-1/2]$, where the parameter $b\approx 2.9$. Even though there is significant scatter of the data, the exponential increase of $\Lambda_{zz}(u)$ with increasing "order parameter" $n_{\parallel}(u)/n_o-1/2$ is clearly discernible. Simultaneously, we observe a less pronounced decrease of the orthogonal thermal conductivity components. The line on the left side in Fig. 11 merely is simple linear least-squares fit to the data. The exponential increase of $\Lambda_{zz}(u)$ indicates that, in addition to the increasing number of monomers oriented in stretch direction, there also must be an enhanced coupling between the excitations on the individual chain segments. It is worth noting that Liu and Yang in Ref. [8] do also observe the same behavior, i.e., an exponential increase of the thermal conductivity in the direction of stretch, in a system of randomly coiled polyethylene chains (cf. Fig. 7 in their paper).

Figure 12 shows the temperature dependence of the thermal conductivity for $u=0$. We have simulated three systems, one without sulfur cross links and two additional ones containing 500 and 1200 disulfide bonds, respectively. The overall temperature dependence of $\bar{\Lambda}$ is rather weak. In addition, within the temperature interval over which the simulation results are obtained, there is only a slight average increase with increasing cross-link density, i.e., $\bar{\Lambda}=0.0582$,0.0584, and 0.0638 W/(mK) for 0,9.4, and 22.6 phr, respectively (where of course the error bars are larger then the observed differences). This increase can be explained as being due to the enhanced coupling of the above deformation modes on neighboring chains. The effect as such is in qualitative agreement with the conclusion in Carwile and Hoge [20], where the authors do find an average increase of the thermal conductivity of 2% per 10 phr increase of the sulfur. (We note that Ni *et al.* [13] in their simulation study of thermal conductance across polyethylene-solid interfaces do find a much more pronounced dependence on the cross-link density.) Quantitatively, however, the experimental data differ considerably from the simulation results. Carwile and Hoge [20] review essentially all thermal conductivity data obtained on natural rubber up to 1966. Overall, also the experimental data differ significantly. Carwile and Hoge discuss these references and reach the conclusion that the curves shown here for soft and hard rubber are the most reliable. With respect to the difference to our simulation results, we can only speculate that

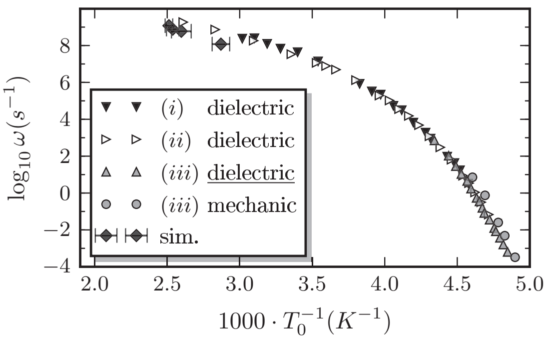

FIG. 13. Relation between frequency and temperature of the segment relaxation peak (α process) for polyisoprene. The simulated points are compared to results obtained via dielectric spectroscopy [(i), (ii), (iii)] as well as mechanical measurements (iii). Experimental molecular weights are between 97.0 kg mol^{-1} and 504.0 kg mol^{-1}. This figure is taken from Meyer *et al.* [39].

these differences may be due to possible additives enhancing the thermal conductivity of the compound.

Finally, we want to address the issue of frequency. As we point out above, the stretching of the samples in the simulations occurs at frequencies of around 10 GHz. In order to connect these high frequencies to the experimentally relevant limit of vanishing frequency, we can make use of temperature-time superposition. Meyer *et al.* [39] have tracked the position of the segment relaxation peak (α process) in an almost identical polymer system. The only differences are that the number of monomers per chain is 200 and the sulfur content is about 14 phr. These simulation results are shown in Fig. 13 including experimental results obtained with different methods.

The simulation data points are obtained by measuring the drag force on and the attendant dissipative loss of a spherical silica nanoparticle while it undergoes a cyclic displacement inside the polymer matrix. The force is measured using a specially designed force gauge, which measures the force on the particle via the extension of a virtual harmonic spring attached at the center of the particle. This measurement in Ref. [39] is obtained as a by-product of simulations aimed at determining the interaction between silica nanoparticles embedded in a polymer matrix.

Even though the simulations cover a comparatively small range, the data tie nicely to the experimental data. Thus the figure permits us to relate the simulation results via the temperature-time-superposition principle to technically more relevant frequencies. We notice that in the present case we must subtract roughly 190 K from the temperature in the simulation to obtain the corresponding experimental temperature in the limit of vanishing frequency. It is important to note that the measurement of the thermal conductivity itself requires a very short time interval only (cf. Figs. 6 and 7); i.e., this measurement is quite independent of the strain rate applied in our simulations.

But what is the significance of the temperature-time or temperature-frequency superposition in the present context? Figure 12 shows that the thermal conductivity depends on temperature only slightly. The experimental conductivity changes by about 10% over the entire temperature range above the glass transition. In Fig. 13 this temperature range corresponds to three decades in frequency. If we apply this to thermal conductivity, then we expect a similarly small change when the strain frequency is lowered by three orders of magnitude from the frequency used in our simulation. In Ref. [8] the authors observe a 20% increase of thermal conductivity when they reduce their strain rate from 10^9 Hz to 10^8 Hz; i.e., their rate reduction is much more moderate by comparison. On the other hand, their system contains a large number of loose chain ends, which do affect the dynamical behavior (they also show this by comparing systems with chains of different length).

IV. CONCLUSION

We study the thermal conductivity tensor in an atomistic model of vulcanized cis-1,4-polyisoprene rubber via molecular dynamics simulations. The systems are subjected to volume-conserving uniaxial strain of variable amplitude. Using the Green-Kubo approach we obtain the diagonal components of the thermal conductivity tensor as a function of strain at $T = 300$ K and $P = 1$ bar. We observe an increase of the thermal conductivity in the direction of elongation in overall good accord with experimental data of Tautz [21]. In addition we present results for the thermal conductivity coefficient at zero strain but for a wide range of cross-link densities and temperatures. Here the agreement with experimental data from the literature is qualitative rather than quantitative.

We conduct an analysis of the heat flux autocorrelation functions, including those in a Lennard-Jones system at two different state points and liquid water at ambient conditions. This leads to the conclusion that the thermal conductivity in PI is governed by short-lived phonon modes at low wave numbers due to deformation of the monomers along the polymer backbone. Application of uniaxial strain to the polymer sample causes increased orientation of monomers along the strain direction. This in turn enhances the thermal conductivity in this direction, whereas a simultaneous decline of thermal conductivity is observed in the orthogonal directions. Specifically, we find an exponential increase of the conductivity in stretch direction in terms of an attendant orientation order parameter. Increasing the cross-link density in the unstrained system yields (on average) a slight increase of the thermal conductivity. Qualitatively this is in accord with experimental data. A more noticeable increase in response to higher cross-link density is observed when strain is applied, but only at the highest stresses. This increase cannot be attributed to orientation but appears to be due to enhanced coupling between chains.

APPENDIX A: DERIVATION OF THE GREEN-KUBO RELATION

The following derivation of the Green-Kubo relation, used here to compute the thermal conductivity tensor elements $\Lambda_{\alpha\beta}$, is primarily based on the (macroscopic) transport equation

$$J_\alpha(\vec{r},t) = -\Lambda_{\alpha\beta}\partial_\beta \delta T(\vec{r},t) = -V\frac{\Lambda_{\alpha\beta}}{C_V}\partial_\beta \delta e(\vec{r},t) \quad \text{(A1)}$$

in conjunction with the continuity equation

$$\partial_\alpha J_\alpha(\vec{r},t) = -\partial_t \delta e(\vec{r},t), \tag{A2}$$

where

$$\delta e(\vec{r},t) = \sum_{i=1}^{N} \delta e_i(t)\delta(\vec{r} - \vec{r}_i(t)). \tag{A3}$$

Here $J_\alpha(\vec{r},t)$ is the α component of the heat current inside a volume element at position $\vec{r}$ and at time t inside the volume V. This current occurs in response to $\delta e(\vec{r},t)$, the fluctuation of the internal energy density in the same volume element and at the same time. Notice that the temperature fluctuation $\delta T(\vec{r},t)$ is related to the energy density fluctuation via $C_V/V = \delta e/\delta T$, where C_V/V is the heat capacity per unit volume. In addition we make use of the summation convention.

The $\vec{r}_i$ are atomic positions and $\delta e_i(t)$ is the deviation of the energy of atom i from its expectation value $\langle e_i \rangle$, i.e.,

$$\delta e_i(t) = \frac{1}{2} m_i v_{i,\alpha}(t) v_{i,\alpha}(t) + \frac{1}{2} \sum_{j(\neq i)=1}^{N} u_{ij}(t) - \langle e_i \rangle. \tag{A4}$$

The first term, where m_i is the mass of atom i and $v_{i,\alpha}$ is the α component of its velocity, is the kinetic energy of atom i and the second term is its potential energy due to pair interaction with atoms j. Notice that $\langle e_i \rangle = \frac{1}{N_{\text{steps}}} \sum_{k=1}^{N_{\text{steps}}} e_i(k\,\Delta t)$, where N_{steps} is the total length of the simulation expressed in terms of time steps of size Δt.

(A) First we derive the mean heat current components $J_\alpha(t)$ expressed in atomic quantities: Inserting the Fourier transforms

$$J_\alpha(\vec{r},t) = \frac{1}{(2\pi)^3} \int d^3k \hat{J}_\alpha(\vec{k},t) e^{-ik_\sigma r_\sigma} \tag{A5}$$

and

$$\delta(\vec{r} - \vec{r}_i(t)) = \frac{1}{(2\pi)^3} \int d^3k e^{-ik_\sigma(r_\sigma - r_{i,\sigma}(t))} \tag{A6}$$

into the continuity equation yields

$$-ik_\alpha \hat{J}_\alpha(\vec{k},t) = -\partial_t \sum_{i=1}^{N} \delta e_i(t) e^{ik_\sigma r_{i,\sigma}(t)}. \tag{A7}$$

Next we expand the exponential on the right-hand side, i.e., $\exp[ik_\sigma r_{\sigma,i}(t)] = 1 + ik_\sigma r_{\sigma,i}(t) + O(k^2)$. In conjunction with $\sum_{i=1}^{N} \delta e_i(t) = 0$ and after taking the limit $\vec{k} \to 0$ we obtain

$$\hat{J}_\alpha(0,t) = \partial_t \sum_{i=1}^{N} \delta e_i(t) r_{\alpha,i}(t). \tag{A8}$$

Finally, with $\hat{J}_\alpha(0,t) = \int d^3r J_\alpha(\vec{r},t) = V J_\alpha(t)$ follows the desired result:

$$J_\alpha(t) = \frac{1}{V} \partial_t \sum_{i=1}^{N} \delta e_i(t) r_{\alpha,i}(t). \tag{A9}$$

It is somewhat tedious but straightforward to work out $J_\alpha(t)$ based on Eq. (A4). The result is

$$\begin{aligned} J_\alpha(t) = {} & \frac{1}{V} \sum_{i=1}^{N} v_{\alpha,i}(t) \delta e_i(t) \\ & + \frac{1}{2V} \sum_{\substack{i,j=1 \\ i \neq j}}^{N} r_{\alpha,ij}(t) f_{\beta,ij}(t) v_{\beta,i}(t). \end{aligned} \tag{A10}$$

Notice that $f_{\beta,ij}$ is the β component of the force on atom i due to atom j.

(B) The derivation of the actual Green-Kubo relation utilizes the $\vec{k}$-space representations of the continuity equation combined with the transport equation:

$$\begin{aligned} ik_\alpha \hat{J}_\alpha(\vec{k},t) &= \delta\dot{\hat{e}}(\vec{k},t) \\ &= -\frac{V}{C_V} k_\alpha k_\beta \Lambda_{\alpha\beta} \delta\hat{e}(\vec{k},t) \equiv -\Lambda \delta\hat{e}(\vec{k},t). \end{aligned} \tag{A11}$$

Here the dot indicates the derivative with respect to time. In addition it is useful to define the Laplace transform

$$\tilde{S}(\vec{k},\omega) \equiv \int_0^\infty dt \hat{S}(\vec{k},t) e^{-\omega t}, \tag{A12}$$

where

$$\hat{S}(\vec{k},t) \equiv \langle \delta\hat{e}(\vec{k},t) \delta\hat{e}(-\vec{k},0) \rangle. \tag{A13}$$

Thus we may write

$$\begin{aligned} -\Lambda \tilde{S}(\vec{k},\omega) &\overset{(A12),(A11)}{=} \int_0^\infty dt \dot{\hat{S}}(\vec{k},t) e^{-\omega t} \\ &= \underbrace{\big|_0^\infty \hat{S}(\vec{k},t) e^{-\omega t}}_{=-\hat{S}(\vec{k},0)} - \underbrace{\int_0^\infty dt \hat{S}(\vec{k},t)(-\omega) e^{-\omega t}}_{=-\omega\tilde{S}(\vec{k},\omega)}. \end{aligned} \tag{A14}$$

And therefore

$$\tilde{S}(\vec{k},\omega) = \frac{\hat{S}(\vec{k},0)}{\omega + \Lambda}. \tag{A15}$$

Next we use (A11), i.e.,

$$\begin{aligned} \Lambda^2 \hat{S}(\vec{k},t) &\overset{(A11),(A13)}{=} \langle \delta\dot{\hat{e}}(\vec{k},t) \delta\dot{\hat{e}}(-\vec{k},0) \rangle \\ &= k_\alpha k_\beta \langle \hat{J}_\alpha(\vec{k},t) \hat{J}_\beta(-\vec{k},0) \rangle. \end{aligned} \tag{A16}$$

Integration of both sides with respect to time yields

$$\Lambda^2 \underbrace{\int_0^\infty dt\ \hat{S}(\vec{k},t)}_{=\tilde{S}(\vec{k},0) \overset{(A15)}{=} \Lambda^{-1} \hat{S}(\vec{k},0)} = k_\alpha k_\beta \int_0^\infty dt\ \langle \hat{J}_\alpha(\vec{k},t) \hat{J}_\beta(-\vec{k},0) \rangle. \tag{A17}$$

Thus

$$\Lambda_{\alpha\beta} \hat{S}(\vec{k},0) = \frac{C_V}{V} \int_0^\infty dt\ \langle \hat{J}_\alpha(\vec{k},t) \hat{J}_\beta(-\vec{k},0) \rangle \tag{A18}$$

and in the limit $\vec{k} \to 0$

$$\Lambda_{\alpha\beta} \hat{S}(0,0) = \frac{C_V}{V} V^2 \int_0^\infty dt\ \langle J_\alpha(t) J_\beta(0) \rangle. \tag{A19}$$

Notice that

$$\hat{S}(0,0) = \langle \delta\hat{e}(0,0)\delta\hat{e}(0,0)\rangle.$$

Using

$$\delta\hat{e}(\vec{k},t) = \int d^3r\delta e(\vec{r},t)\exp[ik_\sigma r_\sigma]$$

we have

$$\hat{S}(0,0) = \int d^3rd^3r'\langle\delta e(\vec{r},0)\delta e(\vec{r}\,',0)\rangle = k_BT^2C_V \quad \text{(A20)}$$

and therefore

$$\Lambda_{\alpha\beta} = \frac{V}{k_BT^2}\int_0^\infty dt\,\langle J_\alpha(t)J_\beta(0)\rangle. \quad \text{(A21)}$$

APPENDIX B: EFFICIENT EVALUATION OF THE AUTOCORRELATION FUNCTION

Autocorrelation functions of the type

$$\begin{aligned}\langle J_\alpha(t)J_\beta(0)\rangle &= \langle J_\alpha(k\Delta t)J_\beta(0)\rangle\\ &= \frac{1}{n-k}\sum_{i=0}^{n-k} J_\alpha((i+k)\Delta t)J_\beta(i\Delta t) \quad \text{(B1)}\end{aligned}$$

are computed efficiently via the following $O(n\log(n))$ algorithm using **DFT** (discrete Fourier transform) or **FFT** (fast Fourier transform). Here Δt is the time step. Expressing Eq. (B1) in matrix form, using $a_i \equiv J_\alpha(i\Delta t)$ and $b_i \equiv J_\beta(i\Delta t)$, we have

$$\begin{pmatrix}\langle a_0b_0\rangle\\ \langle a_1b_0\rangle\\ \vdots\\ \langle a_{n-1}b_0\rangle\end{pmatrix} = \begin{pmatrix}\frac{1}{n} & 0 & \cdots & 0\\ 0 & \frac{1}{n-1} & \cdots & 0\\ \vdots & \vdots & \ddots & \vdots\\ 0 & 0 & \cdots & 1\end{pmatrix} \times \begin{pmatrix}a_0 & a_1 & \cdots & a_{n-1}\\ a_1 & a_2 & \cdots & 0\\ \vdots & \vdots & \ddots & \vdots\\ a_{n-1} & 0 & \cdots & 0\end{pmatrix}\begin{pmatrix}b_0\\ b_1\\ \vdots\\ b_{n-1}\end{pmatrix}. \quad \text{(B2)}$$

Multiplication with the diagonal matrix is an $O(n)$, whereas the matrix-vector product requires $O(n^2)$ multiplications. The computational effort is significantly reduced using the convolution theorem for circulant matrices **Z**, which is common in signal processing, i.e.,

$$\vec{a}\,' * \vec{b}\,' = \mathbf{Z}\vec{b}\,' \Leftrightarrow$$

$$\mathbf{DFT}(\vec{a}\,' * \vec{b}\,') = \mathbf{DFT}(\vec{a}\,') \odot \mathbf{DFT}(\vec{b}\,') = \mathbf{DFT}(\mathbf{Z}\vec{b}\,').$$

This yields

$$\mathbf{Z}\vec{b}\,' = \mathbf{iDFT}(\mathbf{DFT}(\vec{a}\,') \odot \mathbf{DFT}(\vec{b}\,')), \quad \text{(B3)}$$

where the operation $\odot$ means a component-wise multiplication. Because the above convolution requires circulant matrices, we must transform the matrix in Eq. (B2) accordingly:

$$\mathbf{Z} = \begin{pmatrix}a_0 & \cdots & a_{n-1} & 0 & \cdots & 0\\ \vdots & \ddots & \vdots & \vdots & \ddots & \vdots\\ a_{n-1} & \cdots & 0 & 0 & \cdots & a_{n-2}\\ 0 & \cdots & 0 & a_0 & \cdots & a_{n-1}\\ \vdots & \ddots & \vdots & \vdots & \ddots & \vdots\\ 0 & \cdots & a_{n-2} & a_{n-1} & \cdots & 0\end{pmatrix}.$$

The first row in each new column is shifted by one element to the left. Choosing

$$\vec{b}\,' = (b_0, \quad \ldots, \quad b_{n-1}, \quad 0, \quad \ldots, \quad 0)^t$$

yields for $\mathbf{Z}\vec{b}\,'$ the first n elements of the matrix multiplication in (B2). The choice

$$\vec{a}\,' = (a_0, \quad 0, \quad \ldots, \quad 0, \quad a_{n-1}, \quad \ldots, \quad a_1)^t$$

yields the same result if it is determined via (B3). We remark that the result is invariant with respect to cyclic permutation of the components of $\vec{a}\,'$ to the left, provided the same number of cyclic permutations to the right are applied to $\vec{b}\,'$. Notice that the computational effort of the **DFT** is reduced via the *divide et impera* algorithm (**FFT**) from $O(n^2)$ to $O(n\log(n))$.

---

[1] C. L. Choy, W. H. Luk, and F. C. Chen, Thermal conductivity of highly oriented polyethylene, Polymer **19**, 155 (1978).

[2] J.-S. Wang and B. Li, Intriguing Heat Conduction of a Chain with Transverse Motions, Phys. Rev. Lett. **92**, 074302 (2004).

[3] A. Henry and G. Chen, High Thermal Conductivity of Single Polyethylene Chains Using Molecular Dynamics Simulations, Phys. Rev. Lett. **101**, 235502 (2008).

[4] G.-J. Hu, B.-Y. Cao, and Y.-W. Li, Thermal conduction in a single polyethylene chain using molecular dynamics simulations, Chin. Phys. Lett. **31**, 086501 (2014).

[5] Y.-p. Lin, M.-y. Zhang, Y.-f. Gao, L.-y. Mei, Y.-z. Fu, and Y.-q. Liu, Effect of stretching on the thermal conductivity of single polyethylene chains by molecular dynamics simulations, Acta Polymerica Sinica **6**, 789 (2014).

[6] E. Lussetti, T. Terao, and F. Müller-Plathe, Nonequilibrium molecular dynamics calculation of the thermal conductivity of amorphous polyamide-6,6, J. Phys. Chem. B **111**, 11516 (2007).

[7] E. A. Algaer, M. Alaghemandi, M. C. Böhm, and F. Müller-Plathe, Anisotropy of the thermal conductivity of stretched amorphous polystyrene in supercritical carbon dioxide studied by reverse nonequilibrium molecular dynamics simulations, J. Phys. Chem. B **113**, 14596 (2009).

[8] J. Liu and R. Yang, Tuning the thermal conductivity of polymers with mechanical strains, Phys. Rev. B **81**, 174122 (2010).

[9] J. Zhao, J.-W. Jiang, N. Wei, Y. Zhang, and T. Rabczuk, Thermal conductivity dependence on chain length in amorphous polymers, J. Appl. Phys. **113**, 184304 (2013).

[10] M. Alaghemandi, M. R. Garib-Zahedi, E. Spohr, and M. C. Böhm, Thermal conductivity of polyamide-6,6 in the vicinity of charged and uncharged graphene layers: A molecular dynamics analysis, J. Phys. Chem. C **116**, 14115 (2012).

[11] H. Eslami, L. Mohammadzadeh, and N. Mehdipour, Anisotropic heat transport in nanoconfined polyamide-6,6 oligomers:

Atomistic reverse nonequilibrium molecular dynamics simulation, J. Chem. Phys. **136**, 104901 (2012).

[12] E. Rossinsky and F. Müller-Plathe, Anisotropy of the thermal conductivity in a crystalline polymer: Reverse nonequilibrium molecular dynamics simulation of the δ phase of syndiotactic polystyrene, J. Chem. Phys. **130**, 134905 (2009).

[13] B. Ni, T. Watanabe, and S. R. Phillpot, Thermal transport in polyethylene and at polyethylene? Diamond interfaces investigated using molecular dynamics simulation, J. Phys.: Condens. Matter **21**, 084219 (2009).

[14] V. Varshney, S. S. Patnaik, A. K. Roy, and B. L. Farmer, Heat transport in epoxy networks: A molecular dynamics study, Polymer **50**, 3378 (2009).

[15] Y. He, L.-X. Ma, Y.-Z. Tang, Z.-P. Wang, W. Li, and D. Kukulka, Thermal conductivity of natural rubber using molecular dynamics simulation, J. Nanosci. Nanotechnol. **15**, 3244 (2015).

[16] E. A. Algaer and F. Müller-Plathe, Molecular dynamics calculations of the thermal conductivity of molecular liquids, polymers, and carbon nanotubes, Soft Mater. **10**, 42 (2012).

[17] C. E. Barnett, Thermal properties of rubber compounds I. Thermal conductivity of rubber and rubber compounding materials, Ind. Eng. Chem. **26**, 303 (1934).

[18] T. M. Dauphinee, D. G. Ivey, and H. D. Smith, The thermal conductivity of elastomers under stretch and at low temperatures, Can. J. Res. **28a**, 596 (1950).

[19] D. R. Anderson, Thermal conductivity of polymers, Chem. Rev. **66**, 677 (1966).

[20] L. C. K. Carwile and H. J. Hoge, Thermal conductivity of soft vulcanized natural rubber: Selected values, Rubber Chem. Technol. **39**, 126 (1966).

[21] H. Tautz, Das Verhalten der Wärmeleitfähigkeit von Kautschuk bei der Dehnung, Kolloid-Z. **174**, 128 (1961).

[22] D. Hands and F. Horsfall, The thermal diffusivity and conductivity of natural rubber compounds, Rubber Chem. Technol. **50**, 253 (1977).

[23] D. Hands, The effect of biaxial orientation on the thermal conductivity of vulcanized and unvulcanized rubber, Rubber Chem. Technol. **53**, 80 (1980).

[24] T. Bhowmick and S. Pattanayak, Thermal conductivity, heat capacity and diffusivity of rubbers from 60 to 300K, Crogenics **30**, 116 (1990).

[25] V. A. Harmandaris, M. Doxastakis, V. G. Mavrantzas, and D. N. Theodorou, Detailed molecular dynamics simulation of the self-diffusion of *n*-alkane and cis-1,4 polyisoprene oligomer melts, J. Chem. Phys. **116**, 436 (2002).

[26] J. Hager, R. Hentschke, N. W. Hojdis, and H. A. Karimi-Varzaneh, Computer simulation of particle-particle interaction in a model polymer nanocomposite, Macromolecules **48**, 9039 (2015).

[27] S. Pronk, S. Páll, R. Schulz, P. Larsson, P. Bjelkmarand, R. Apostolov, M. R. Shirtsand, J. C. Smith, M. P. Kasson, D. van der Spoel, B. Hess, and E. Lindahl, GROMACS 4.5: A high-throughput and highly parallel open source molecular simulation toolkit, Bioinformatics **29**, 845 (2013).

[28] A. T. McPherson, *Density and electrical properties of the system*, rubber-sulphur. Part I. Density of rubber-sulphur compounds (U. S. Dept. of Commerce, Bureau of Standards, Washington, D. C., 1927).

[29] W. D. Cornell, P. Cieplak, C. I. Bayly, I. R. Gould, K. M. Merz, Jr., D. M. Ferguson, D. C. Spellmeyer, T. Fox, J. W. Caldwell, and P. A. Kollmann, A second generation force field of proteins, nucleic acids, and organic molecules, J. Am. Chem. Soc. **117**, 5179 (1995).

[30] J. A. Becker *et al.* (private communication).

[31] M. Doxastakis, V. G. Mavrantzas, and D. N. Theodorou, Atomistic Monte Carlo simulation of cis-1,4 polyisoprene melts. I. Single temperature end-bridging Monte Carlo simulations, J. Chem. Phys. **115**, 11339 (2001).

[32] J. O. Hirschfelder, C. F. Curtis, and R. B. Bird, *Molecular Theory of Gases and Liquids* (John Wiley and Sons, New York, 1954).

[33] H. J. C. Berendsen, J. R. Grigera, and T. P. Straatsma, The missing term in effective pair potentials, J. Chem. Phys. **91**, 6269 (1987).

[34] J. L. F. Abascala and C. Vega, A general purpose model for the condensed phases of water: TIP4P/2005, J. Chem. Phys. **123**, 234505 (2005).

[35] M. W. Mahoney and W. L. Jorgensen, A five-site model for liquid water and the reproduction of the density anomaly by rigid, nonpolarizable potential functions, J. Chem. Phys. **112**, 8910 (2000).

[36] P. L. Silvestri, M. Bernasconi, and M. Parrinello, *Ab initio* infrared spectrum of liquid water, Chem. Phys. Lett. **277**, 478 (1997).

[37] B. Tonpheng, J. Yu, and O. Andersson, Thermal Conductivity, heat capacity, and cross-linking of polyisoprene/single-wall carbon nanotube composites under high pressure, Macromolecules **42**, 9295 (2009).

[38] P. Nallasamy and S. Mohan, Vibrational spectra of cis-1,4-polyisoprene, Arabian J. Sci. Eng. **29**, 17 (2004).

[39] J. Meyer, R. Hentschke, J. Hager, N. W. Hojdis, and H. A. Karimi Varzane, Molecular simulation approach to the prediction of mechanical properties of silica reinforced rubbers, Macromolecules (to be published).